Zero-point averaged dynamics of Ar n + He 1000 : Dopant-size influence on potential-energy surfaces, mass spectra and fragmentation patterns

David A Bonhommeau

To cite this version:

David A Bonhommeau. Zero-point averaged dynamics of Ar n + He 1000 : Dopant-size influence on potential-energy surfaces, mass spectra and fragmentation patterns. Chemical Physics, 2021, 550, pp.111307. ⟨10.1016/j.chemphys.2021.111307⟩. ⟨hal-03844453⟩

HAL Id: hal-03844453
https://hal.science/hal-03844453v1

Submitted on 8 Nov 2022

Zero-point averaged dynamics of $\mathrm{Ar}_n^+\mathrm{He}_{1000}$: Dopant-size influence on potential-energy surfaces, mass spectra and fragmentation patterns

David A. Bonhommeau*

Université de Reims Champagne Ardenne, CNRS, GSMA UMR 7331, 51097 Reims, France.

Abstract

The fragmentation of $\mathrm{Ar}_n^+\mathrm{He}_{1000}$ ($n = 3, 5$) is investigated by zero-point averaged dynamics (ZPAD) and compared with recent results on $\mathrm{Ar}_4^+\mathrm{He}_{1000}$ to investigate the influence of the dopant size. At the core of ZPAD, effective He-He potentials converged for He_{1000} and $\mathrm{Ar}_n\mathrm{He}_{1000}$ are found alike which suggests that ZPAD simulations on argon-doped helium nanodroplets (HNDs) could restrict to effective potentials obtained for pure HNDs. The fragmentation dynamics of $\mathrm{Ar}_n^+\mathrm{He}_{1000}$ clusters share a number of similarities, like the absence of Ar^+-containing fragments, the occurrence of ion ejections and trappings, Ar_n^+ electronic relaxation typically extending on a picosecond time scale, or primary fragmentation events which are not necessarily representative of the final distribution of fragments. However, $\mathrm{Ar}_3^+\mathrm{He}_{1000}$ clusters also exhibit unexpected behaviors like an inefficient electronic relaxation when the dynamics starts on the uppermost Ar_3^+ electronic state which makes the dopant trapped within the droplet.

Keywords: mixed quantum-classical dynamics, helium nanodroplets, argon clusters, zero-point energy, ion ejection, ion trapping, recombination.

---

1. Introduction

Although the first observation of helium nanodroplets (HNDs) by Becker and colleagues dates back to the 1960's [1], the doping of HNDs with clusters or molecules only emerged thirty years later. Among the first dopants to be considered were rare-gas clusters, ideal systems to investigate the capture and coagulation of species within HNDs [2, 3, 4], the physical processes behind the dopant ionization after bombarding the surface of the doped HND with electrons [5, 6] or high-energy photons [7, 8], and the subsequent fragment distributions, signature of the fragmentation mechanisms at play. Beside the

---

[*] Corresponding author, Email: david.bonhommeau@univ-reims.fr

common observation of progressions of peaks steadily spaced out by 4 u, mass-spectrometry experiments also demonstrated the existence of "magic numbers", namely sizes of particularly stable fragments, for all common rare-gas clusters although these anomalies were less abundant and intense for xenon than for argon or krypton [9, 10]

On the theoretical side, the modeling of doped HNDs confronts with the need for describing large systems ($N = 10^3 - 10^6$ in typical experiments) of quantum nature. Takayanagi and Shiga tackled the photodissociation of Cl_2 in helium clusters composed of 200 atoms by combining a wavepacket dynamics for Cl_2 with a path-integral molecular dynamics of helium nuclei. Chlorine dissociated in most of trajectories, a result later confirmed by Vilá et al. who carried out TDDFT simulations on Cl_2He_{500} [11]. In an attempt to free from the nanodroplet size, Bonhommeau et al. adopted a phenomenological description of helium atoms represented as a friction force that applied to the dopant, a neon cluster, when its speed exceeded the Landau critical velocity [12]. Despite some qualitative agreement with experiments regarding the size of neon fragments, this method was not suited to discuss helium evaporation, magic numbers, or fragmentation mechanisms, and a more explicit method remained to be devised.

In this context, Bonhommeau et al. proposed another approach called zero-point averaged dynamics (ZPAD) to investigate the fragmentation of $Ne_n^+He_{100}$ clusters ($n = 4 - 6$) [13, 14]. The cornerstone of this method is the design of an effective He-He interaction potential that takes into account zero-point effects in an average manner. By combining this effective potential with the dopant potential-energy surface and dopant-He interactions, the mixed quantum-classical dynamics of the doped HND can be achieved at reasonable computational cost. Simulations on neon-doped HNDs proved the existence of fast ion ejections [14], a fragmentation process which also resulted in the ejection of helium atoms with kinetic energies of $\sim 28 - 45\,\mathrm{cm}^{-1}$, well above the typical binding energy of a helium atom to the HND (~ 5 cm^{-1}) [3]. The smallness of the cluster prevented any observation of trappings or recombinations since abundances of ionic fragments mostly converged after a few tens of picoseconds due to ion ejections. In contrast, recent ZPAD simulations on $Ar_4^+He_{1000}$ demonstrated the occurrence of a multitude of fragmentation patterns, from fast ion ejections, favored by high electronic excitations of the dopant, to long-term ion trappings, favored by low electronic excitations of the dopant [15]. Geminate recombinations were also identified as a source of Ar_3^+ and Ar_4^+ fragments although the electronic relaxation of the initially excited Ar_4^+ dopant mainly produced Ar_2^+. No Ar^+-containing fragments were found whereas such fragments are abundant in experimental mass spectra [10], which seemed to indicate that such fragments might come from HNDs doped with smaller dopants (eg, Ar_3^+), more prone to dissociate into Ar^+ in the gas phase [16], secondary ionizations of large Ar_pHe_q fragments [15], or multiple ionization of the initial HND.

In the present paper, ZPAD simulations are carried out on $Ar_n^+He_{1000}$ ($n = 3, 5$). The essential features of the ZPAD approach applied to argon-doped HNDs are first recalled in Section 2. In the same section, effective He-He interaction potentials converged for He_{1000}, Ar_3He_{1000}, and Ar_5He_{1000} are compared with each other and with the effective He-He potential recently obtained for Ar_4He_{1000} to evaluate the influence of the dopant size on these potentials. Mass spectra and fragmentation patterns of $Ar_n^+He_{1000}$ ($n = 3 - 5$) are then discussed in terms of dopant size and initial electronic excitation in Section 3. Concluding remarks about the influence of superfluidity on the results and possible improvements of ZPAD to model the dynamics of argon-doped, and more generally rare-gas-doped, HNDs are collected in Section 4.

2. Method

2.1. Origin of ZPAD

In the mid-1990's Sterling et al. proposed to model the dynamics of solid parahydrogen, pure or doped with Li, by describing H_2 molecules as gaussian particles [17]. For this purpose, they constructed an average interaction potential for solid H_2 by convolving a reference potential with a gaussian function which represented the H_2 probability density [17]. Slavíček et al. later generalized this approach to investigate the photodissociation dynamics of hydrogen halides in floppy neon clusters by iteratively calculating the neon wave function rather than assuming it of gaussian type [18]. Ne-Ne effective potentials were then fully converged after as few as four iterations. ZPAD is a direct extension of the method introduced by Slavíček et al. to HNDs doped with rare-gas clusters. It encompasses two methods: an iterative procedure devoted to the construction of an effective He-He interaction potential representative of the neutral doped HND (potential part of ZPAD), and the subsequent mixed quantum-classical dynamics of the neutral and ionized doped HNDs based on this effective potential (dynamical part of ZPAD). A comprehensive presentation of ZPAD is provided in our previous publications on neon- and argon-doped HNDs [13, 14, 15] and we mainly recall here essential features of the method.

2.2. Potential part of ZPAD

In the case of argon-doped HNDs, the reference system used to build the effective He-He interaction potential is Ar_nHe_{1000} ($n \leq 5$). The corresponding potential-energy surface is

$$V_{\mathrm{neut}}(\mathbf{R}) = \sum_{i=1}^{n} \sum_{\substack{j=1 \\ j>i}}^{n} V_{\mathrm{Ar-Ar}}(R_{ij}) + \sum_{i=1}^{n} \sum_{a=1}^{1000} V_{\mathrm{He-Ar}}(R_{ia}) + \sum_{a=1}^{1000} \sum_{\substack{b=1 \\ b>a}}^{1000} V_{\mathrm{He-He}}(R_{ab}) \tag{1}$$

where $V_{\mathrm{Ar-Ar}}(R)$ is the HFDID1 Ar-Ar potential [19], $V_{\mathrm{He-Ar}}(R)$ is the HFD-B He-Ar potential proposed by Keil et al. [20, 21], and $V_{\mathrm{He-He}}(R)$ is the SAPT2 He-He potential built by Janzen and Aziz [22].

The first step of the iterative potential part of ZPAD is a molecular dynamics (MD) equilibration at $T = 0.38\,\mathrm{K}$ [23] for 3 ns (3×10^5 steps of 10 fs carried out with a velocity verlet algorithm), the last nanosecond being devoted to the calculation of the classical He-He radial distribution function (rdf). In every iteration except iteration 1, this classical rdf is convolved with the squared helium wavefunction from the previous iteration, then yielding a less structured semiclassical rdf that includes quantum effects. The convolution of the SAPT2 He-He potential with the rdf (classical for iteration 1 and semiclassical otherwise) then enables the formation of the average radial potential felt by one helium atom in the mean field due to the others. This radial potential serves as input in a radial Schrödinger equation that can be variationally solved by using a basis set composed of sine functions or Laguerre polynomials. The squared eigenfunction is finally convolved with the SAPT2 He-He potential to produce an effective He-He potential. This procedure, from equilibration to effective potential generation, is then repeated until convergence is achieved [18].

Effective He-He potentials obtained for He_{1000}, $\mathrm{Ar}_3\mathrm{He}_{1000}$, and $\mathrm{Ar}_5\mathrm{He}_{1000}$ are depicted in Figure 1. A truncation of helium wavefunctions at 1.6 Å was required during the iterative procedure because of the high zero-point energy of helium clusters that made convergence hard to reach. About thirty iterations were needed to get an energy deviation lower than 10^{-3} cm^{-1} between the well depths of two successive effective He-He potentials. Data points for these potentials were fitted on the following analytical form:

$$V^{\mathrm{eff}}_{\mathrm{He-He}} = V_{\mathrm{rep}}(R) + T(R)\left[V_{\mathrm{well}}(R) - V_{\mathrm{rep}}(R)\right], \tag{2}$$

where

$$\begin{aligned} V_{\mathrm{rep}}(R) &= A\exp\left[-\alpha_1 R/R_e - \alpha_2 (R/R_e)^2\right], && \text{(3a)} \\ V_{\mathrm{well}}(R) &= \sum_{i=3}^{6} c_{2i}(R/R_e)^{-2i}, && \text{(3b)} \\ T(R) &= 0.5(1+\tanh[a(R-b)]). && \text{(3c)} \end{aligned}$$

$V_{\mathrm{well}}(R)$ reproduces accurately the well and long-range part of the potential while $V_{\mathrm{rep}}(R)$ is added to better model the repulsive wall and $T(R)$ is a switching function. The fitting parameters of the effective potentials obtained for He_{1000}, $\mathrm{Ar}_3\mathrm{He}_{1000}$, and $\mathrm{Ar}_5\mathrm{He}_{1000}$ are reported in Table 1. Standard deviations (SD) between data points and the fitted analytical function remain below 0.003 cm^{-1} in the region of negative energies (SD$^-$) and do not exceed 0.72 cm^{-1} in the region of positive energies (SD$^+$), which corresponds to the repulsive part of the potential. Moreover, according to Figure 1a, all the effective potentials have very similar shapes, and their well depths and equilibrium distances differ by less than 0.05 cm^{-1} and 0.04 Å, respectively. Therefore, Ar_n dopants seem to have little influence on effective He-He potentials, a result that should hold true for larger HNDs. Indeed, the larger the droplet, the smaller the influence of a given dopant on the average He-He radial potential. This observation suggests that ZPAD could be fed by effective He-He potentials representative of pure HNDs, all the more since effective potentials obtained for $\mathrm{Ar}_n\mathrm{He}_{1000}$ are probably not more relevant to model the fragmentation dynamics of the ionic system than those converged for pure HNDs.

However, the potential part of ZPAD suffers from several limitations. Firstly, it is only suitable for large helium clusters ($N \gtrsim 100$) for which defining an average rdf and radial potential is relevant. Secondly, as illustrated in Figure 1, the He-He well depth is about 1.3 cm^{-1} which means that very small clusters, and especially ions detected in mass spectra, could be more stable than in experiments. This latter drawback might not have a significant influence on the results since the cohesion of small ions is governed by dopant-He rather than He-He interactions, then making the smallest ions solid-like. In particular, Bartl et al found magic numbers for $\mathrm{Ar^+He}_q$ (q = 12, 32 and 44) interpreted as icosahedral layers about Ar^+ [10]. Similarly, Döppner et al found magic numbers for $\mathrm{Ag^+He}_q$ (q = 10, 12, 32 and 44) when investigating silver-doped droplets, although they had not discussed the structure of the corresponding fragments [24].

2.3. Dynamical part of ZPAD

$\mathrm{Ar}_n\mathrm{He}_{1000}$ is first equilibrated for at least 10 ps on the potential-energy surface presented in Eq.(1) where the SAPT2 He-He potential is replaced by the newly converged effective He-He potential. The ionization by electron bombardment is then modeled as a white-light vertical ionization that excites similarly the $3n$ electronic states of the Ar_n^+ dopant, these states being calculated by diagonalizing a diatomics-in-molecules (DIM) matrix [25, 26]. The mixed quantum-classical dynamics of $\mathrm{Ar}_n^+\mathrm{He}_{1000}$ is achieved by coupling a surface-hopping technique for Ar_n^+, the molecular dynamics with quantum transitions (MDQT) method [27, 28], with a classical dynamics of helium atoms. The dynamics of the ion starts on a randomly selected potential-energy surface j

$$V_{\mathrm{ion}}^j(\mathbf{R}) = V_j + V^j_{\mathrm{He-Ar_n^+}} + \sum_{a=1}^{1000}\sum_{\substack{b=1\\b>a}}^{1000} V^{\mathrm{eff}}_{\mathrm{He-He}}(R_{ab}), \tag{4}$$

where

$$V^j_{\mathrm{He-Ar_n^+}} = \sum_{i=1}^{n}\sum_{a=1}^{1000}\left[q_i^{(j)}\overline{V}_{\mathrm{He-Ar^+}}(R_{ia}) + \left(1-q_i^{(j)}\right)V_{\mathrm{He-Ar}}(R_{ia})\right]. \tag{5}$$

In Eq.(4), V_j is the jth DIM adiabatic energy of Ar_n^+ and $\overline{V}_{\mathrm{He-Ar^+}}$ is a weighted sum of the analytical functions proposed by Carrington et al. for the $\mathrm{X}^2\Sigma^+$ and $\mathrm{A}^2\Pi$ electronic states of He-Ar$^+$ [29]. The multisurface nature of the system is taken into account by allowing for hops between Ar_n^+ adiabatic surfaces. These hops influence the delocalization of the charge carried by Ar_n^+ and, subsequently, the couplings between the dopant and helium atoms in Eq.(5). Velocity adjustment at a hopping event is achieved along the direction of $\mathbf{g}_{\mathrm{He}} = \nabla(V^k_{\mathrm{He-Ar_n^+}} - V^j_{\mathrm{He-Ar_n^+}})$ where j and k are the indices of the two surfaces involved in the hop. This nonadiabatic dynamics is performed for 100 ps to enable electronic relaxation of the system and it is followed by a 400-ps adiabatic dynamics.

3. Results

3.1. Fragment abundances

Theoretical mass spectra obtained for $\mathrm{Ar}_3^+\mathrm{He}_{1000}$ and $\mathrm{Ar}_5^+\mathrm{He}_{1000}$ at $t = 500\,\mathrm{ps}$ are plotted in Figure 2. They are typically composed of a narrow set of peaks at low masses ($m \lesssim 200\,\mathrm{u}$), a broad distribution of peaks at masses $200\,\mathrm{u} \lesssim \mathrm{m} \lesssim 3500\,\mathrm{u}$, and another narrow set of peaks at masses close to the parent ion mass ($m \gtrsim 4000\,\mathrm{u}$). The two first peak distributions were recently discussed within the context of the fragmentation dynamics of $\mathrm{Ar}_4^+\mathrm{He}_{1000}$ [15]: The lower-mass peaks were attributed to fast ion ejections while higher masses mainly corresponded to ion trappings in droplets composed of hundreds of helium atoms. However, the analysis of $\mathrm{Ar}_4^+\mathrm{He}_{1000}$ trajectories for several cutoff radii and velocity adjustment techniques had not revealed significant amounts of ions with masses close to the parent ion mass. Such trajectories are also rare in $\mathrm{Ar}_5^+\mathrm{He}_{1000}$ calculations but they represent roughly 14% of $\mathrm{Ar}_3^+\mathrm{He}_{1000}$ trajectories. Among these trajectories, $\sim 80\%$ started on the most excited Ar_3^+ electronic state (ie, state 9 in our state numbering). This point is worth noting because the highest-energy excited state of Ar_3^+ is expected to contribute significantly to the production of Ar^+ fragments in the gas phase [16] and the trapping of excited Ar_3^+ consequently harms the formation of $\mathrm{Ar}^+\mathrm{He}_q$ fragments. To ensure that discrepancies between $\mathrm{Ar}_3^+\mathrm{He}_{1000}$ and $\mathrm{Ar}_5^+\mathrm{He}_{1000}$ mass spectra are not artifacts induced by our choice of velocity adjustment vector at hopping events, additional 160 trajectories are performed for these two systems along the direction of $\mathbf{g}_{\mathrm{kj}} = \nabla(V_k - V_j)$, namely the gradient of the energy difference between the two Ar_n^+ adiabatic states involved in the hop [30, 31, 32]. As depicted in Figure S1, the same trends arise on the new mass spectra, then confirming the results obtained for $\mathbf{g}_{\mathrm{He}}$.

While assigning an experimental peak to the corresponding species requires high-resolution mass spectrometers [10], this information can be easily extracted from ZPAD simulations. The contributions of the many ionic fragments to the total mass spectra of $\mathrm{Ar}_n^+\mathrm{He}_{1000}$ ($n = 3 - 5$) are depicted with color bars in Figure 3, where distinct colors are assigned to ionic fragments with respect to the size of their Ar_p^+ ionic core ($p \leq n$). Note that data obtained for $\mathrm{Ar}_4^+\mathrm{He}_{1000}$ are also reported because such an analysis had not been completely performed in our former publication on this system [15]. For a given value of p, $\mathrm{Ar}_p^+\mathrm{He}_q$ ($p \leq n$) fragments are sorted into four groups: bare ions ($q = 0$), small ions ($0 < q \leq 50$), medium-sized ions ($50 < q \leq 500$) and large ions ($q > 500$). This sorting yields 16 families of $\mathrm{Ar}_p^+\mathrm{He}_q$ fragments whose average abundances are plotted as insets in Figure 3.

The fragmentation of $\mathrm{Ar}_3^+\mathrm{He}_{1000}$ produces $\mathrm{Ar}_2^+\mathrm{He}_q$ in 71% of the trajectories, half of these fragments corresponding to small ions ($q \leq 50$). The remaining 29% of the trajectories yield $\mathrm{Ar}_3^+\mathrm{He}_q$, three fourths of these fragments corresponding to large ions ($q > 500$). As expected from gas-phase data [16, 33] where larger argon clusters tend to form larger ionic fragments, the proportion of $\mathrm{Ar}_3^+\mathrm{He}_q$ coming from $\mathrm{Ar}_4^+\mathrm{He}_{1000}$ or $\mathrm{Ar}_5^+\mathrm{He}_{1000}$ fragmentation ($\sim 29\%$ and 37%, respectively) increases at the expense of the abundance of $\mathrm{Ar}_2^+\mathrm{He}_q$ ($\sim 65\%$ and 40%, respectively) and fragments with larger ionic cores (ie, $Ar_4^+He_q$ and $Ar_5^+He_q$) emerge ($\sim$ 5% and 23%, respectively).

Moreover, for all $Ar_n^+He_{1000}$ parent ions investigated here, Ar_p^+ ionic cores ($p \geq 3$) of large helium clusters ($q > 500$) are rather slightly bound complexes connecting an Ar_2^+ ion with Ar atoms (eg, $Ar_2^+ \cdots Ar$) than compact Ar_p^+ clusters. Indeed, the average Ar-Ar distance is much larger than expected for compact Ar_p^+ ionic cores. It reaches ~ 9 Å for Ar_3^+ ionic cores (~ 9.4 Å for $Ar_3^+He_{1000}$ and $Ar_4^+He_{1000}$, and ~ 8.5 Å for $Ar_5^+He_{1000}$), ~ 12 Å for Ar_4^+ ionic cores (~ 13.3 Å for $Ar_4^+He_{1000}$ and ~ 10.1 Å for $Ar_5^+He_{1000}$) and ~ 13.1 Å for Ar_5^+ ionic cores. On the contrary, the Ar-Ar distance in Ar_2^+ ionic cores is about 2.45 Å (~ 2.56 Å for $Ar_3^+He_{1000}$, ~ 2.45 Å for $Ar_4^+He_{1000}$, and ~ 2.35 Å for $Ar_5^+He_{1000}$), in agreement with the equilibrium distance of the gas phase dimer in its ground electronic state [34]. As pointed out elsewhere [15], the formation of such slightly bound complexes can be attributed to limitations of the effective He-He potentials, that remains too deep to reproduce perfectly liquid helium, to helium snowballs about argon atoms, and to the neglect of superfluidity in ZPAD simulations.

No fragments containing an Ar^+ ionic core are formed during the fragmentation process of $Ar_n^+He_{1000}$. This result would intuitively suggest that Ar^+He_q ($q < 1000$) produced by single ionization of a HND should only come from smaller dopants (ie, Ar or Ar_2) unless the inclusion of spin-orbit couplings drastically modifies theoretical fragment abundances, a point that will be tackled in future works. However, Figure S2 shows that large $ArHe_q$ and Ar_2He_q clusters can form during the fragmentation of $Ar_n^+He_{1000}$ and an additional ionization of these species, which is not modeled here, would increase the abundance of small Ar^+He_q fragments with no requirement for initial HNDs doped with Ar or Ar_2. Moreover, HNDs are typically composed of $10^5 - 10^6$ helium atoms in recent experiments using rare gases as dopants [9, 10] and ions produced upon ionization of $ArHe_N$ or Ar_2He_N ($N = 10^5 - 10^6$) might be too large to appear on experimental mass spectra whose mass range has an upper limit. Thence, the origin of small Ar^+He_q fragments in experiments is not clear and would need further investigation.

The lack of Ar^+He_q fragments and the large abundance of bare ions (Ar_2^+ and Ar_3^+) in our simulations together with the limited number of trajectories (160 per system) make impossible any quantitative comparison with experimental magic numbers. However, we can evaluate whether some $Ar_p^+He_q$ fragments ($2 \leq p \leq 5$, $1 \leq q < 1000$) produced frequently (in at least 5 trajectories) correspond to identified magic numbers. For $Ar_n^+He_{1000}$ parent ions, common fragments are Ar_2^+He and $Ar_2^+He_{10}$ when $n = 3$, Ar_2^+He and $Ar_2^+He_2$ when $n = 4$, Ar_2^+He, $Ar_2^+He_6$ and $Ar_3^+He_4$ when $n = 5$. The closest experimental magic numbers are $Ar_2^+He_7$, $Ar_2^+He_{12}$, and $Ar_3^+He_8$ [10]. This disagreement confirms the need for making the statistics on a much broader range of HND and dopant sizes, a larger number of trajectories, and longer times all the more since we cannot exclude that some of the aforementioned $Ar_p^+He_q$ fragments would have only increased the abundance of Ar_2^+ and Ar_3^+ if ZPAD simulations had been extended beyond the 500-ps time limit.

3.2. Fragmentation patterns

The sudden ionization of the embedded neutral argon cluster, whose structure is far from the global minimum structure of the ionic species, makes the dopant dissociate. The average time needed for electronic relaxation of the dopant is depicted in Figure 4a as a function of the initial state number j (see Eq.(4)). The average DIM energies of initial states j are also displayed for the sake of completeness. For $Ar_5^+He_{1000}$, the electronic relaxation is completed within at most $\sim 2\,ps$ when ZPAD starts on one of the thirteen lower-energy states while it can last up to $\sim 40\,ps$ when the highest-energy state is excited. A similar behavior is observed for $Ar_4^+He_{1000}$, the highest-energy state leading to a relaxation time of $\sim 30\,ps$. However, this behavior contrasts with that observed for $Ar_3^+He_{1000}$. Although the relaxation time increases with energy up to states $5-6$, it decreases sharply for states 7 and 8 and no data is available for state 9 since all the trajectories starting on this state remained blocked in an excited state after 100 ps, which also explains why these trajectories correspond to trapped ions with masses close to the parent ion mass (see Section 3.1). A qualitative explanation for the faster electronic relaxation from states 7 and 8 can be inferred from Figures 4b and S3 where the nonadiabatic dynamics of Ar_3^+ and Ar_5^+ excited electronic states are illustrated. For Ar_5^+ the decay to the ground state is slower for the higher-energy states, then following the energy ordering of excited states. For Ar_3^+, this behavior is roughly maintained up to state 6. In fact, it appears that the coupling of states 7 and 8 with states 5 and 6 is efficient while the coupling from these states to lower states (states 1 to 4) is weaker, as suggested by the plateaus observed for states 5 and 6 below $t = 2\,ps$ in Figure 4b. However, the decay of states 7 and 8 to the lowest-energy states seems to benefit from the kinetic energy gained during the preliminary decay to states 5 and 6, reminding that the probability for surface hops depends on the scalar product between nonadiabatic coupling vectors and atomic velocities. Such a behavior is not observed for larger dopants and should rely on the equilateral geometry of the Ar_3 precursor.

Upon completion of the dopant electronic relaxation, an ion can be ejected from the HND or trapped within the droplet. In this context, fragmentation processes can be sorted into three main families [15]: (i) fast ejections of small ions ($Ar_p^+He_q$ with $p < n$ and $q \leq 50$) within the first 100 ps of the dynamics, (ii) long-term trappings where a large ion ($Ar_p^+He_q$ with $p \leq n$ and $q > 500$) slowly loses helium atoms by evaporation on long time scales ($t > 500\,ps$), and (iii) intermediate processes encompassing all other kinds of processes like delayed ejections ($t > 100\,ps$), trappings in smaller droplets ($q \leq 500$), or ejections mediated by cycles of trappings and recombinations. A statistics of trajectories subject to these three types of fragmentation processes is reported in Figure 5 for $Ar_n^+He_{1000}$ ($n = 3$ and 5). It is clear that trappings are always favored by the low-energy excitations whereas fast ejections are favored by high energies, which confirms results recently obtained for $Ar_4^+He_{1000}$ [15]. A slight deviation occurs for intermediate processes whose distribution of trajectories is rather uniform in the case of $Ar_4^+He_{1000}$ while a peak arises at mid-range energies in calculations devoted to $Ar_3^+He_{1000}$ and $Ar_5^+He_{1000}$. However, this feature would require confirmation by increasing the number of trajectories for the three above-mentioned systems.

Point-cloud diagrams in Figures 5c and 5d confirm that fast ejections rather produce small ions while large ions especially come from long-term trappings, intermediate processes filling the mass range in between. Nevertheless, a few cases deserve more attention, namely large $Ar_2^+He_q$ and small $Ar_4^+He_q$ produced by fast ejections (see red circles at $m \approx 400\,\mathrm{u}$ and $m \approx 1850\,\mathrm{u}$ in Figure 5c and red triangles in Figure 5d). Trajectory inspection reveals that the ionic fragment with mass $m \approx 400\,\mathrm{u}$ comes from the fast ejection of a rotating $Ar_2^+He_2$ fragment with little translational energy that is captured by the burst HND in its path to form a smaller compact droplet. Ar_2^+ recombines with the trapped argon atom to form Ar_3^+ and eventually produces an $Ar_2^+He_{80}$ fragment because of the energy released by the geminate recombination that makes helium atoms evaporate. Masses at $m \approx 1850\,\mathrm{u}$ follow a simpler pattern where and Ar_2^+ ion, possibly surrounded by a few helium atoms, is ejected and captured by the burst HND to form and $Ar_2^+He_q$ cluster with $m \approx 440\,\mathrm{u}$. Finally, small $Ar_4^+He_q$ fragments typically come from the swift ejection of an argon atom leaving an Ar_4^+ or $Ar_3^+ \cdots Ar$ behind. Then, the trapped ion can be ejected as an $Ar_4^+He_q$ fragment ($q \lesssim 10$) due to the recoil energy of the primarily ejected argon atom or the geminate recombination of the slightly bound Ar_3^+ and Ar subsystems. Similar fragmentation patterns were also observed for $Ar_4^+He_{1000}$ [15]. Such examples illustrate the great variety of fragmentation processes at play and the fact that a comprehensive understanding of the primary fragmentation events induced by the dopant ionization is not sufficient to account for final fragment abundances.

4. Conclusion

Zero-point averaged dynamics (ZPAD) of doped HNDs are based on the construction of an effective He-He interaction potential representative of the neutral droplet. Similarities between effective potentials converged for He_{1000} and Ar_nHe_{1000} made us conclude that focusing on the pure HND should be sufficient to get reliable results. This observation is essential because convergence of a single potential may need one month with the procedure followed for Ar_nHe_{1000}, each and every iteration being checked before running the next iteration. Therefore, it opens new avenues toward simulations of large doped HNDs provided that the dopant potential-energy surface is known.

In the case of $Ar_n^+He_{1000}$ ($n = 3-5$) a number of similarities emerge, from the absence of Ar^+He_q fragments in mass spectra to the occurrence of fast ion ejections and long-term ion trappings, although some discrepancies may arise when focusing on details, like the uppermost Ar_3^+ electronic state that does enable electronic relaxation within the first 100 ps of the dynamics. The comparison of these results with experimental data remains limited by the number of trajectories (∼10-20 by Ar_n^+ electronic state), the short time scale ($t_{max} = 0.5\,\mathrm{ns}$) that precludes any completion of helium evaporation, and the fact that experimental spectra are averaged over an unknown distribution of HND and dopant sizes.

In recent mass-spectrometry experiments the largest fragments reported contain up to eight argon atoms [10] which defines a lower limit for the maximum size of the Ar_n dopant. From our results and gas-phase data [16, 33], we can reasonably infer that applying the current ZPAD approach to $\mathrm{Ar}_n^+\mathrm{He}_{1000}$ ($6 \leq n \lesssim 10$) should not yield different trends: fragmentation patterns should be alike, $\mathrm{Ar}^+\mathrm{He}_q$ fragments should not form, and the abundance of fragments with large Ar_p^+ ionic cores ($p \geq 3$) should increase at the expense of $\mathrm{Ar}_2^+\mathrm{He}_q$ fragments. Comparisons with experiments may however be harmed by the neglect of superfluidity in ZPAD. Indeed, this property is expected to be relevant at two stages of the experiments: (i) during the capture and coagulation of argon atoms by the pure HND, a physical process which is not modeled here, and (ii) at long times ($\gtrsim$ 1ns) when cooled doped HNDs may subsist and undergo recombinations of embedded argon atoms. For instance, a molecular beam with speed 500 m s^{-1} crossing an ionization chamber of 10 cm long is exposed to high-energy electrons for 0.2 ms. Putting aside the possibility for multiple ionization of the HND, this time is much longer than the 0.5 ns of current ZPAD simulations. In other words, even if superfluidity is not taken into account, argon atoms embedded in small HNDs ($100 \lesssim N < 1000$) modeled with ZPAD might have enough time to recombine and release small ions in the gas phase if simulations are extended to experimental time scales. However, this does not involve that the subsequent distribution of ions would be exactly the same as that obtained in experiments using the same droplet sizes.

Beside the question of superfluidity, ZPAD can be refined by constructing more fluid-like effective He-He potentials for pure HNDs closer to experimental sizes ($N = 10^3 - 10^6$), by performing simulations beyond the nanosecond time scale to model the slow helium evaporation, and by including spin-orbit couplings in the DIM matrix representative of Ar_n^+ dopants. The latter improvement would make the matrix complex-valued [35, 36], double the number of electronic states, and require the rewriting of MDQT equations [37] since nonadiabatic coupling vectors will be complex-valued. We could also construct effective He-Ar potentials in complement to He-He ones, an improvement which has not be done here for the sake of comparison with previous calculations performed on $\mathrm{Ar}_4^+\mathrm{He}_{1000}$. All these refinements are currently considered to improve ZPAD and make it more versatile.

5. Supplementary material

Theoretical mass spectra of $\mathrm{Ar}_3^+\mathrm{He}_{1000}$ and $\mathrm{Ar}_5^+\mathrm{He}_{1000}$ at $t = 500$ ps averaged over 160 trajectories when using $\mathbf{g_{kj}}$ as velocity adjustment vector (Figure S1). Average number of neutral fragments per trajectory at t = 500 ps for $\mathrm{Ar}_n^+\mathrm{He}_{1000}$ ($n = 3 - 5$) parent ions (Figure S2). Nonadiabatic dynamics of Ar_5^+ excited electronic states (Figure S3).

6. Data Availability Statement

The data that support the findings of this study are available from the corresponding author upon reasonable request.

7. Acknowledgments

Prof. Marius Lewerenz is gratefully acknowledged for providing me with the set of routines devoted to the convergence of the effective He-He potential-energy curves. Dr Nadine Halberstadt is warmly acknowledged for fruitful discussions and strong interest in this work.

References

[1] E. W. Becker, On the History of Cluster Beams, Z. Phys. D 3 (1986) 101–107.

[2] A. Scheidemann, J. P. Toennies, J. A. Northby, Capture of Neon Atoms by ^{4}He Clusters, Phys. Rev. Lett. 64 (1990) 1899–1902.

[3] M. Lewerenz, B. Schilling, J. P. Toennies, Successive capture and coagulation of atoms and molecules to small clusters in large liquid helium clusters, J. Chem. Phys. 102 (1995) 8191–8207.

[4] B. E. Callicoatt, K. Förde, T. Ruchti, L. Jung, K. C. Janda, N. Halberstadt, Capture and ionization of argon within liquid helium droplets, J. Chem. Phys. 108 (1998) 9371–9382.

[5] T. Ruchti, K. Förde, B. E. Callicoatt, H. Ludwigs, K. C. Janda, Charge transfer and fragmentation of liquid helium clusters that contain one or more neon atoms, J. Chem. Phys. 109 (1998) 10679–10687.

[6] T. Ruchti, B. E. Callicoatt, K. C. Janda, Charge transfer and fragmentation of liquid helium droplets doped with xenon, Phys. Chem. Chem. Phys. 2 (2000) 4075–4080.

[7] R. Fröchtenicht, U. Henne, J. P. Toennies, A. Ding, M. Fieber-Erdmann, T. Drewello, The photoionization of large pure and doped helium droplets, J. Chem. Phys. 104 (1996) 2548–2556.

[8] J. H. Kim, D. S. Peterka, C. C. Wang, D. M. Neumark, Photoionization of helium nanodroplets doped with rare gas atoms, J. Chem. Phys. 124 (2006) 214301.

[9] P. Bartl, S. Denifl, P. Scheier, O. Echt, On the stability of cationic complexes of neon with helium - solving an experimental discrepancy, Phys. Chem. Chem. Phys. 15 (2013) 16599–16604.

[10] P. Bartl, C. Leidlmair, S. Denifl, P. Scheier, O. Echt, On the Size and Structure of Helium Snowballs Formed around Charged Atoms and Clusters of Noble Gases, J. Phys. Chem. A 118 (2014) 8050–8059.

[11] A. Vilà, M. González, R. Mayol, Photodissociation Dynamics of Homonuclear Diatomic Molecules in Helium Nanodroplets. The Case of $Cl_2@(^4He)_N$, J. Chem. Theory Comput. 11 (2015) 899–906.

[12] D. Bonhommeau, N. Halberstadt, A. Viel, Fragmentation dynamics of ionized neon clusters (Ne_n, $n = 3$ to 14) embedded in helium nanodroplets, J. Chem. Phys. 124 (2006) 024328.

[13] D. Bonhommeau, P. T. Lake, Jr., C. L. Quiniou, M. Lewerenz, N. Halberstadt, Modeling the fragmentation dynamics of ionic clusters inside helium nanodroplets: The case of $He_{100}Ne_4^+$, J. Chem. Phys. 126 (2007) 051104.

[14] D. Bonhommeau, M. Lewerenz, N. Halberstadt, Fragmentation of ionized doped helium nanodroplets: Theoretical evidence for a dopant ejection mechanism, J. Chem. Phys. 128 (2008) 054302.

[15] N. Halberstadt, D. A. Bonhommeau, Fragmentation dynamics of Ar_4He_{1000} upon electron impact ionization: Competition between ion ejection and trapping, J. Chem. Phys. 152 (2020) 234305.

[16] D. Bonhommeau, N. Halberstadt, A. Viel, Fragmentation dynamics of argon clusters (Ar_n, $n = 2$ to 11) following electron impact ionization: Modeling and comparison with experiment, J. Chem. Phys. 124 (2006) 184314.

[17] M. Sterling, Z. Li, V. A. Apkarian, Simulations of quantum crystals by classical dynamics, J. Chem. Phys. 103 (1995) 5679–5683.

[18] P. Slavíček, P. Jungwirth, M. Lewerenz, N. H. Nahler, M. Fárník, U. Buck, Pickup and Photodissociation of Hydrogen Halides in Floppy Neon Clusters, J. Phys. Chem. A 107 (2003) 7743–7754.

[19] R. A. Aziz, A highly accurate interatomic potential for argon, J. Chem. Phys. 99 (1993) 4518–4525.

[20] M. Keil, L. J. Danielson, P. J. Dunlop, On obtaining interatomic potentials from multiproperty fits to experimental data, J. Chem. Phys. 94 (1991) 296–309.

[21] C. Douketis, G. Scoles, S. Marchetti, M. Zen, A. J. Thakkar, Intermolecular forces via hybrid Hartree-Fock-SCF plus damped dispersion (HFD) energy calculations. An improved spherical model, J. Chem. Phys. 76 (1982) 3057–3063.

[22] A. R. Janzen, R. A. Aziz, An accurate potential energy curve for helium based on ab initio calculations, J. Chem. Phys. 107 (1997) 914–919.

[23] S. Grebenev, J. P. Toennies, A. F. Vilesov, Superfluidity Within a Small Helium-4 Cluster: The Microscopic Andronikashvili Experiment, Science 279 (1998) 2083–2086.

[24] T. Döppner, T. Diederich, S. Göde, A. Przystawik, J. Tiggesbäumker, K.-H. Meiwes-Broer, Ion induced snowballs as a diagnostic tool to investigate the caging of metal clusters in large helium droplets, J. Chem. Phys. 126 (2007) 244513.

[25] W. R. Wadt, The geometry and spectral properties of Ne_3^+, Ar_3^+, Kr_3^+, and Xe_3^+, Appl. Phys. Lett. 38 (1981) 1030.

[26] P. J. Kuntz, J. Valldorf, A DIM model for homogeneous noble gas ionic clusters, Z. Phys. D 8 (1988) 195–208.

[27] J. C. Tully, Molecular dynamics with electronic transitions, J. Chem. Phys. 93 (1990) 1061–1071.

[28] S. Hammes-Schiffer, J. C. Tully, Proton transfer in solution: Molecular dynamics with quantum transitions, J. Chem. Phys. 101 (1994) 4657–4667.

[29] A. Carrington, C. A. Leach, A. J. Marr, A. M. Shaw, M. R. Viant, J. M. Hutson, M. M. Law, Microwave spectroscopy and interaction potential for the longrange $He\cdots Ar^+$ ion, J. Chem. Phys. 102 (1995) 2379–2403.

[30] N. C. Blais, D. G. Truhlar, Trajectory-surface-hopping study of $Na(3p\ ^2P) + H_2 \to Na(3s\ ^2S) + H_2(v', j', \theta)$, J. Chem. Phys. 79 (1983) 1334–1342.

[31] N. C. Blais, D. G. Truhlar, C. A. Mead, The effect of a conical intersection on cross sections for collision-induced dissociation, J. Chem. Phys. 89 (1988) 6204–6208.

[32] M. D. Hack, A. W. Jasper, Y. L. Volobuev, D. W. Schwenke, D. G. Truhlar, Quantum Mechanical and Quasiclassical Trajectory Surface Hopping Studies of the Electronically Nonadiabatic Predissociation of the $\tilde{\mathrm{A}}$ State of NaH_2, J. Phys. Chem. A 103 (1999) 6309–6326.

[33] D. Bonhommeau, N. Halberstadt, U. Buck, Fragmentation of rare-gas clusters ionized by electron impact: New theoretical developments and comparison to experiments, Int. Rev. Phys. Chem. 26 (2007) 353–390.

[34] T. K. Ha, P. Rupper, A. Wüest, F. Merkt, The lowest electronic states of Ne_2^+, Ar_2^+ and Kr_2^+: comparison of theory and experiment, Mol. Phys. 101 (2003) 827–838.

[35] J. S. Cohen, B. Schneider, Ground and excited states of Ne_2 and Ne_2^+. I. Potential curves with and without spin-orbit coupling, J. Chem. Phys. 61 (1974) 3230–3239.

[36] M. Amarouche, G. Durand, J. P. Malrieu, Structure and stability of Xe_n^+ clusters, J. Chem. Phys. 88 (1988) 1010–1018.

[37] D. Bonhommeau, Dynamique de fragmentation d'agrégats de gaz rares monochargés en phase gazeuse et à l'intérieur de nanogouttes d'hélium, Ph.D. thesis, Université Toulouse III - Paul Sabatier (2006).

Table 1: Parameters of the effective He-He interaction potentials converged for He_{1000}, $\mathrm{Ar}_3\mathrm{He}_{1000}$, and $\mathrm{Ar}_5\mathrm{He}_{1000}$ with a wave function cutoff radius $R_{\mathrm{cut}} = 1.6\,\text{Å}$.

Parameters	He_{1000}	$\mathrm{Ar}_3\mathrm{He}_{1000}$	$\mathrm{Ar}_5\mathrm{He}_{1000}$
R_e (Å)	4.40136	4.40034	4.39113
A (cm^{-1})	42864.1	1944.72	1942.29
α_1	-0.922778	-7.98855	-8.01035
α_2	13.021	17.2366	17.2557
c_6 (cm^{-1})	-2.41494	-2.34751	-2.35672
c_8 (cm^{-1})	7.72659	7.33127	7.32458
c_{10} (cm^{-1})	-15.5743	-14.8025	-14.8356
c_{12} (cm^{-1})	8.99999	8.53158	8.56887
a (Å^{-1})	41.7872	18.446	18.425
b (Å)	3.56143	3.6181	3.6136

List of Figures

1 (color online) Analytical curves of effective He-He interaction potentials obtained for He_{1000}, Ar_3He_{1000}, Ar_4He_{1000} [15], and Ar_5He_{1000} with a wave function cutoff radius of 1.6 Å(a). Potential energies (black circles) derived from the iterative potential part of ZPAD and corresponding fitted analytical functions (red lines) are plotted for He_{1000} (b), Ar_3He_{1000} (c), and Ar_5He_{1000} (d). Standard deviations (SD) are also indicated for the regions of positive energies ($R \lesssim 4$ Å, SD denoted SD^+) and negative energies ($R \gtrsim 4$ Å, SD denoted SD^-). 18

2 (color online) Theoretical mass spectra of $Ar_3^+He_{1000}$ (a) and $Ar_5^+He_{1000}$ (b) at $t = 500$ ps averaged over 160 trajectories. Results coming from trajectories where the ground electronic state of Ar_n^+ is reached at $t = 100$ ps are represented in red whereas those corresponding to trajectories blocked in an excited electronic state of Ar_n^+ are represented in blue. In insets, black arrows indicate masses where fragments with alike masses yield superimposed peaks due to the figure scale. This case occurs at $m \approx 120$ u (Ar_3^+ and $Ar_2^+He_{10}$), $m \approx 124$ u (Ar_3^+He and $Ar_2^+He_{11}$), $m \approx 164$ u (Ar_4^+He and $Ar_3^+He_{11}$), and $m \approx 172$ u ($Ar_4^+He_3$ and $Ar_3^+He_{13}$). 19

3 (color online) Contributions of $Ar_p^+He_q$ ($2 \leq p \leq 5$, $0 \leq q \leq 1000$) fragments to theoretical mass spectra of $Ar_3^+He_{1000}$ (a), $Ar_4^+He_{1000}$ (b) and $Ar_5^+He_{1000}$ (c) at $t = 500$ ps. Histograms plotted in insets are built by sorting $Ar_p^+He_q$ fragments into families which depend on the dopant size p ($p = 2$: black ; $p = 3$: red ; $p = 4$: blue ; $p = 5$: green) and on the number of surrounding helium atoms q (bare ions: $q = 0$, label B ; small ions: $0 < q \leq 50$, label S ; medium-sized ions: $50 < q \leq 500$, label M ; large ions: $500 < q \leq 1000$, label L). Figure b is partly reproduced from Ref. [15], with the permission of AIP Publishing. 20

4 (color online) Average electronic relaxation time $\langle t_{r,j} \rangle$ of Ar_3^+ (black solid line), Ar_4^+ (black solid line) [15], Ar_5^+ (red solid line) as a function of the initial state number (a) and nonadiabatic dynamics of Ar_3^+ excited electronic states (b). In Figure a, the average initial DIM energies $\langle V_j \rangle$ corresponding to the $3n$ states of the Ar_n^+ dopants are also reported (black squares: Ar_3^+ ; blue squares: Ar_4^+ ; red squares: Ar_5^+). In Figure b, state numbers are averaged over all the trajectories. Figure a is partly reproduced from Ref. [15], with the permission of AIP Publishing. 21

5 (color online) Fraction of trajectories subject to fast ejection of small ionic fragments (red lines), long-term trapping of Ar_p^+ ($2 \leq p \leq 5$, blue lines), or intermediate processes (black lines) as a function of the initial Ar_n^+ ($n = 3$, 5) electronic state number (a and b) and corresponding point-cloud diagrams showing the mass of ionic fragments which contain Ar_2^+ (circles), Ar_3^+ (squares), Ar_4^+ (triangles), and Ar_5^+ (diamonds) (c and d). In plot b, fractions of trajectories are computed by gathering states 1 to 14 by pairs (ie, (1,2), $\cdots$, (13,14)) because of noise on the results related to the limited number of trajectories by electronic state. In point-cloud diagrams, the color of symbols refers to the dynamical process involved to produce the fragments (red: fast ejection; blue: long-term trapping; and black: intermediate process) and trajectories where the Ar_n^+ ground electronic state is reached before $t = 100\,\mathrm{ps}$ are only considered. 22

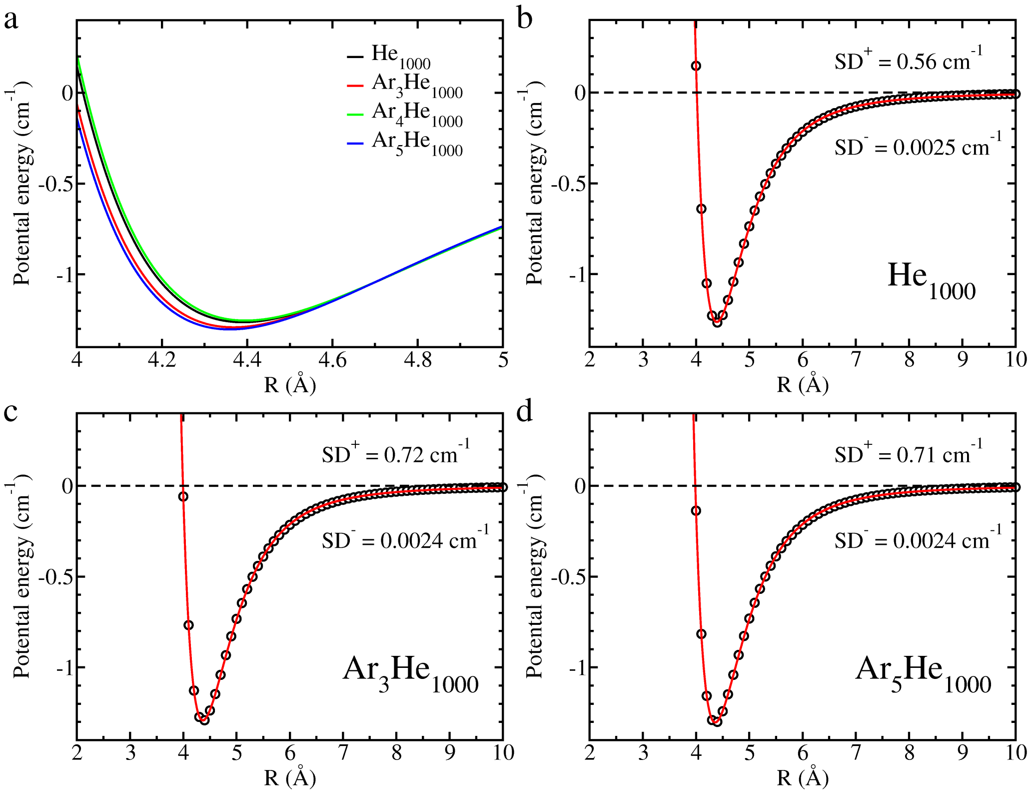

Figure 1: (color online) Analytical curves of effective He-He interaction potentials obtained for He_{1000}, Ar_3He_{1000}, Ar_4He_{1000} [15], and Ar_5He_{1000} with a wave function cutoff radius of 1.6 Å(a). Potential energies (black circles) derived from the iterative potential part of ZPAD and corresponding fitted analytical functions (red lines) are plotted for He_{1000} (b), Ar_3He_{1000} (c), and Ar_5He_{1000} (d). Standard deviations (SD) are also indicated for the regions of positive energies ($R \lesssim 4$ Å, SD denoted SD^+) and negative energies ($R \gtrsim 4$ Å, SD denoted SD^-).

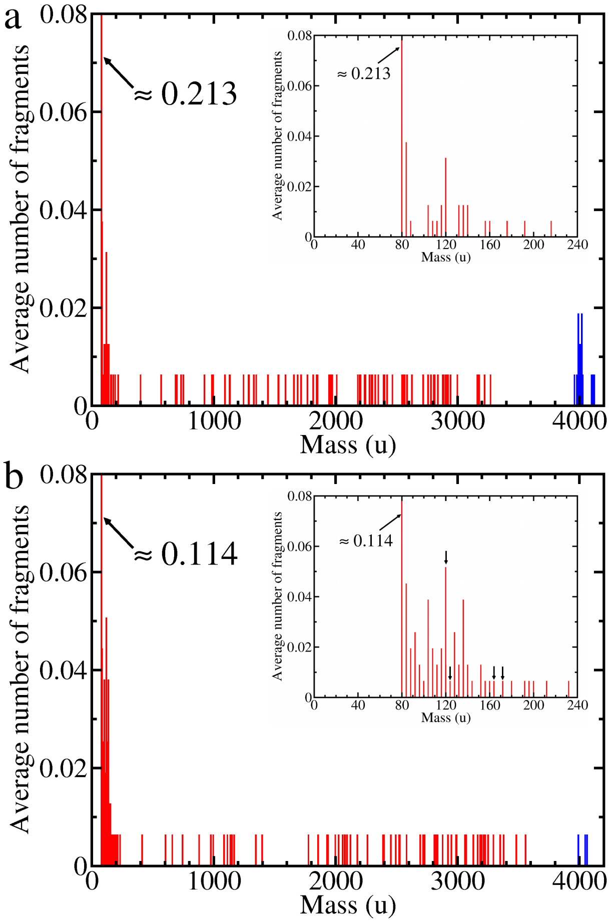

Figure 2: (color online) Theoretical mass spectra of $\mathrm{Ar}_3^+\mathrm{He}_{1000}$ (a) and $\mathrm{Ar}_5^+\mathrm{He}_{1000}$ (b) at $t = 500\,\mathrm{ps}$ averaged over 160 trajectories. Results coming from trajectories where the ground electronic state of Ar_n^+ is reached at $t = 100\,\mathrm{ps}$ are represented in red whereas those corresponding to trajectories blocked in an excited electronic state of Ar_n^+ are represented in blue. In insets, black arrows indicate masses where fragments with alike masses yield superimposed peaks due to the figure scale. This case occurs at $m \approx 120$ u (Ar_3^+ and $\mathrm{Ar}_2^+\mathrm{He}_{10}$), $m \approx 124$ u ($\mathrm{Ar}_3^+\mathrm{He}$ and $\mathrm{Ar}_2^+\mathrm{He}_{11}$), $m \approx 164$ u ($\mathrm{Ar}_4^+\mathrm{He}$ and $\mathrm{Ar}_3^+\mathrm{He}_{11}$), and $m \approx 172$ u ($\mathrm{Ar}_4^+\mathrm{He}_3$ and $\mathrm{Ar}_3^+\mathrm{He}_{13}$).

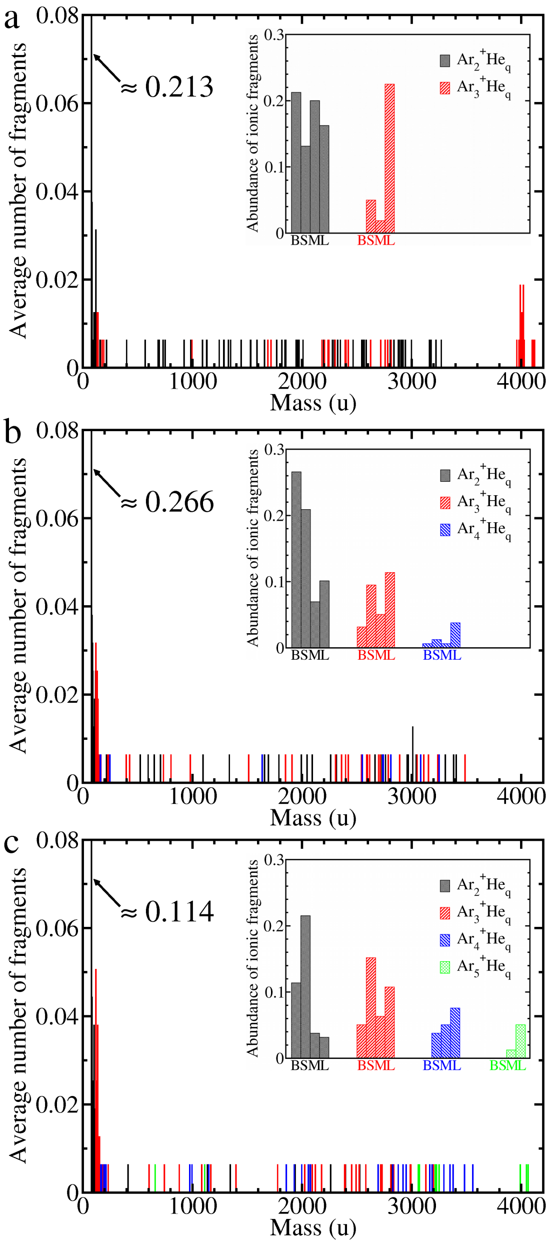

Figure 3: (color online) Contributions of $Ar_p^+He_q$ ($2 \leq p \leq 5$, $0 \leq q \leq 1000$) fragments to theoretical mass spectra of $Ar_3^+He_{1000}$ (a), $Ar_4^+He_{1000}$ (b) and $Ar_5^+He_{1000}$ (c) at $t = 500$ ps. Histograms plotted in insets are built by sorting $Ar_p^+He_q$ fragments into families which depend on the dopant size p ($p = 2$: black ; $p = 3$: red ; $p = 4$: blue ; $p = 5$: green) and on the number of surrounding helium atoms q (bare ions: $q = 0$, label B ; small ions: $0 < q \leq 50$, label S ; medium-sized ions: $50 < q \leq 500$, label M ; large ions: $500 < q \leq 1000$, label L). Figure b is partly reproduced from Ref. [15], with the permission of AIP Publishing.

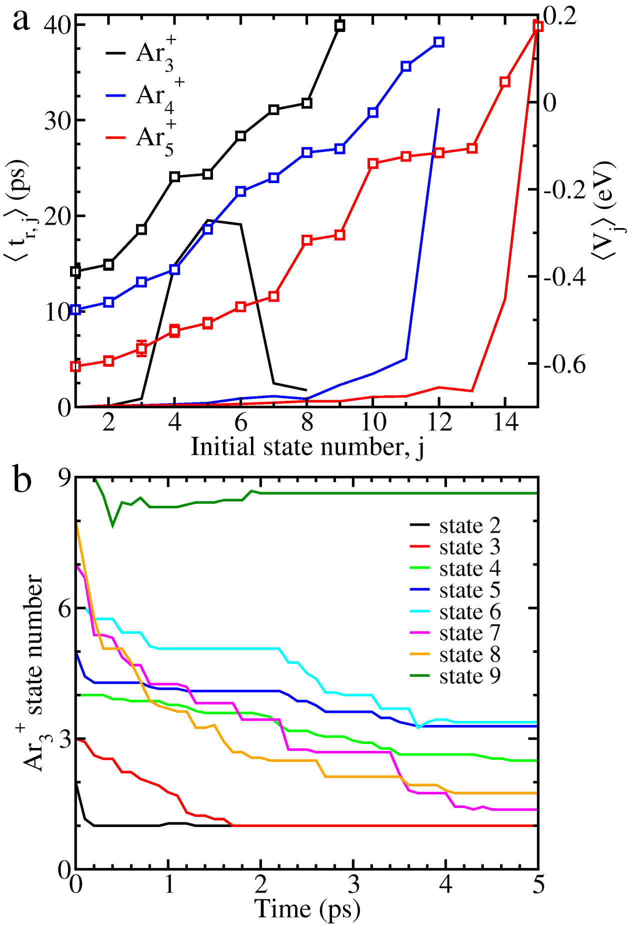

Figure 4: (color online) Average electronic relaxation time $\langle t_{r,j}\rangle$ of Ar_3^+ (black solid line), Ar_4^+ (black solid line) [15], Ar_5^+ (red solid line) as a function of the initial state number (a) and nonadiabatic dynamics of Ar_3^+ excited electronic states (b). In Figure a, the average initial DIM energies $\langle V_j\rangle$ corresponding to the $3n$ states of the Ar_n^+ dopants are also reported (black squares: Ar_3^+ ; blue squares: Ar_4^+ ; red squares: Ar_5^+). In Figure b, state numbers are averaged over all the trajectories. Figure a is partly reproduced from Ref. [15], with the permission of AIP Publishing.

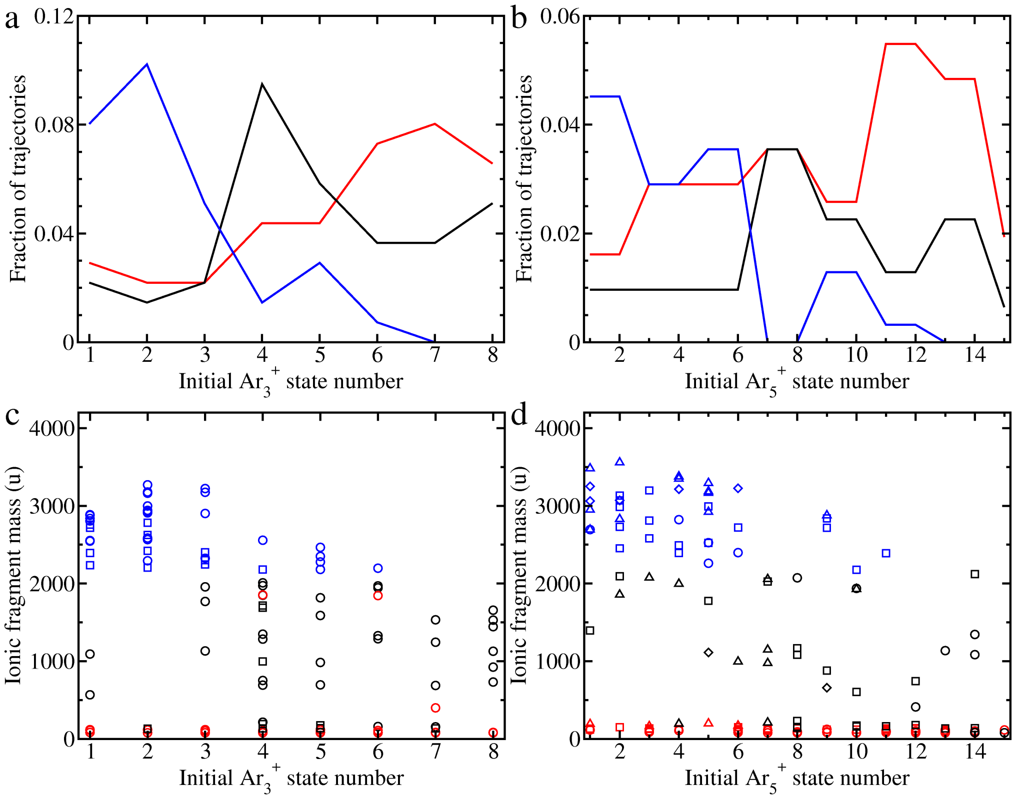

Figure 5: (color online) Fraction of trajectories subject to fast ejection of small ionic fragments (red lines), long-term trapping of Ar_p^+ ($2 \leq p \leq 5$, blue lines), or intermediate processes (black lines) as a function of the initial Ar_n^+ ($n = 3$, 5) electronic state number (a and b) and corresponding point-cloud diagrams showing the mass of ionic fragments which contain Ar_2^+ (circles), Ar_3^+ (squares), Ar_4^+ (triangles), and Ar_5^+ (diamonds) (c and d). In plot b, fractions of trajectories are computed by gathering states 1 to 14 by pairs (ie, (1,2), $\cdots$, (13,14)) because of noise on the results related to the limited number of trajectories by electronic state. In point-cloud diagrams, the color of symbols refers to the dynamical process involved to produce the fragments (red: fast ejection; blue: long-term trapping; and black: intermediate process) and trajectories where the Ar_n^+ ground electronic state is reached before $t = 100\,\mathrm{ps}$ are only considered.